Constraining microphysics assumptions on the modeling of Atmospheric Rivers using GNSS Polarimetric Radio Occultations

Antía Paz[1,2,3], Ramon Padullés[1,2], and Estel Cardellach[1,2]

[1]Institut de Ciències de l'Espai, Consejo Superior de Investigaciones Científicas (ICE-CSIC), Barcelona, Spain
[2]Institut d'Estudis Espacials de Catalunya (IEEC), Barcelona, Spain
[3]Facultat de Física, Universitat de Barcelona (UB), Carrer de Martí i Franquès, 1-11, 08028 Barcelona, Spain

Correspondence: Antía Paz (a.paz@csic.es)

Abstract. The Polarimetric Radio Occultation (PRO) technique enhances the standard Radio Occultation (RO) method by offering vertical profiles of precipitation structure and thermodynamic atmospheric profiles. PRO achieves this by utilizing two orthogonal polarizations—horizontal (H) and vertical (V)—to measure the differential phase shift ($\Delta\Phi$), which represents the difference in phase delay between the two of them. This study focuses on assessing the sensitivity of the PRO technique to the vertical structure of hydrometeors under different microphysical assumptions. To explore this sensitivity, simulations were conducted using the Weather Research and Forecasting (WRF) model, with particular attention to the effects of different microphysics schemes on the simulated $\Delta\Phi$. The study also incorporated the Atmospheric Radiative Transfer Simulator (ARTS) particle database to characterize hydrometeors based on their scattering properties. Atmospheric Rivers (ARs) were used as a case study. The simulated $\Delta\Phi$ values were compared to GNSS-PRO observational data from PAZ and Spire satellites, providing a means to evaluate the performance of the WRF microphysics parameterizations. Combining water content information derived from WRF simulations with ARTS-based scattering parameters, the specific differential phase (K_{dp}) was computed for various hydrometeor types. This allowed for a detailed assessment of their contributions to the observable $\Delta\Phi$. Results indicate that the Goddard and WSM6 schemes are the ones that reproduce better the observations for most of the studied cases. Similarly, snow particle habits that yield a factor of 0.1 between water content and K_{dp} are the ones that lead to a better match between the observations and simulations.

1 Introduction

The Global Navigation Satellite System (GNSS) Radio Occultation (RO) technique is a remote sensing method that tracks signals emitted by navigation satellites (e.g. GPS, Galileo, etc.) from a Low Earth Orbit (LEO) satellite as it rises or sets behind the Earth's limb. This method enables the retrieval of atmospheric refractivity by analyzing the delay and bending of radio signals as they propagate through the atmosphere. As these signals traverse increasingly dense atmospheric layers, they experience bending caused by vertical gradients of the refractive index. This delay can be used to derive profiles of radio refractivity and ionospheric total electron content. From these refractivity profiles, key atmospheric variables such as pressure, temperature, and water vapor pressure can be retrieved, spanning from the stratosphere to the surface with a vertical

resolution of 100–300 meters (e.g., Kursinski et al., 1997). These atmospheric products are operationally assimilated into

25   global Numerical Weather Prediction (NWP) models (e.g., Healy et al., 2005).

The distinction between the standard RO technique and the Polarimetric Radio Occultation (PRO) technique lies in their antenna configurations. While standard RO uses Right Hand Circularly Polarized (RHCP) antennas, the PRO technique employs dual orthogonal polarizations, horizontal (H) and vertical (V). Therefore, the PRO technique offers a novel extension to standard RO by enabling the measurement of differential phase delays caused when the signals interact with nonspherical

30   hydrometeors in the atmosphere (Cardellach et al., 2015). These interactions result in positive differential phase shifts ($\Delta\Phi$), defined as the difference between H and V polarizations, a phenomenon driven by the asymmetry of the hydrometeors. Consequently, PRO not only produces the traditional RO products (vertical profiles of thermodynamic variables), but also provides detailed information on the vertical structure of precipitation on a global scale, becoming the first technique to provide both types of observations simultaneously from the same instrument.

35   Operational testing of the PRO technique began in 2018 with the Spanish LEO satellite PAZ as part of the Radio Occultation and Heavy Precipitation (ROHP) experiment, led by the Institut de Ciéncies de l'Espai-Consejo Superior de Investigaciones Científicas/Institut d'Estudis Espacials de Catalunya (ICE-CSIC/IEEC) in collaboration with the NOAA, UCAR, and NASA/JPL. Since 2023, the technique has also been implemented on three Spire Global CubeSats (Talpe et al., 2025) and two PlanetiQ satellites. PRO's primary objective is the detection of intense precipitation, a capability that has been success-

40   fully demonstrated (Cardellach et al., 2019). Furthermore, it has been shown that PRO is sensitive to both heavy rainfall and horizontally oriented frozen hydrometeors (Padullés et al., 2021, 2023). Validation of the $\Delta\Phi$ observable has been performed using two-dimensional datasets such as the Integrated Multi-satellite Retrievals from GPM (IMERG) (Cardellach et al., 2019; Padullés et al., 2020). Passive microwave radiometers have also been utilized to interpret precipitation vertical structures, (Turk et al., 2021). More recently, three-dimensional data from the Next Generation Weather Radars (NEXRAD) have been used to

45   assess the vertical structure of the measured $\Delta\Phi$ (Paz et al., 2024).

This study aims to assess the use of PRO in constraining microphysical assumptions within models exploiting the sensitivity of the technique to the amount of water content and to particle shapes. These change depending on the assumed microphysics, and may lead to differences in the forecast of relevant magnitudes such as the amount of rainfall. To achieve the objective, simulations will be conducted using the Weather Research and Forecasting (WRF) model with different microphysical pa-

50   rameterizations. The WRF model provides a robust framework for simulating atmospheric phenomena with the flexibility to adjust parameterizations representing key processes within these events (Skamarock et al., 2019). This study will focus on analyzing the impacts of different parameterizations on cloud microphysical processes. Since such small-scale processes cannot be directly resolved by models, we will examine how assumptions regarding microphysical parameterizations influence the simulated $\Delta\Phi$. These simulations will help determine to which extent variations in microphysical schemes can be discerned

55   with PRO observations, as was hypothesized by Murphy et al. (2019) using simulated data.

To simulate the $\Delta\Phi$ observable from PRO, it is necessary to quantify the electromagnetic scattering properties of hydrometeors. However, the microphysical schemes implemented in mesoscale models such as WRF do not explicitly provide the scattering characteristics (e.g., scattering matrices) needed to perform our computation. To address this limitation, we use the

Atmospheric Radiative Transfer Simulator (ARTS) habit database, which provides absorption and extinction coefficients for a

60 wide range of hydrometeor habits. From these coefficients, the relevant scattering parameters can be derived and used to construct a forward operator that links the hydrometeor water content (WC) from WRF outputs to the specific differential phase (K_{dp}). The scattering parameters used to compute $\Delta\Phi$ have been derived in Padullés et al. (2025b) and are publicly available in Padullés et al. (2025c). The use of the ARTS database also ensures consistency with other scientific communities, such as the microwave (MW) remote sensing community, which employ these parameters for assimilation into NWP models, (Geer

65 et al., 2021).

Our study will focus on Atmospheric Rivers (AR). These events are narrow, elongated corridors of concentrated atmospheric moisture transport, often originating in the tropics and extending towards mid-latitudes. They play a critical role in the global water cycle, delivering substantial precipitation when the moisture interacts with topographic features or frontal systems. While ARs contribute to beneficial water supplies, they are also associated with extreme rainfall and flooding, being also responsible

70 of important damage and loss. Their spatial extent enables a large amount of coincidences with PRO observations and allows a systematic study that comprises around 40 cases split in two different regions: the north-east Pacific and the north Atlantic. ARs have been widely studied using standard RO (e.g. Murphy and Haase, 2022) and airborne RO (e.g. Haase et al., 2021), with focus on assessing the assimilation of the standard products in their forecast. By including the information about the cloud processes, we expect that PRO has the potential to go one step further in the improvement of their prediction.

75 This paper is organized as follows: Section 2 describes the data and methodology used in the analysis; Section 3 presents the results of comparisons with PRO observations and the consequent discussion; and Section 4 presents the conclusions.

2 Data and methodology

This section outlines the data sources used for the analysis, including PRO data, WRF outputs, and the ARTS dataset. Additionally, the methodology for defining the forward operator used to calculate the simulated differential phase shift, $\Delta\Phi_{sim}$,

80 will be explained.

2.1 Polarimetric Radio Occultation data

In this analysis, we use PRO data obtained from the PAZ satellite and from the Spire nanosatellites.

As noted previously, the PRO technique enables us to compare the phase delay (Φ) corresponding to two distinct measured polarizations. During heavy precipitation events, large, horizontally oriented raindrops result in a positive accumulated

85 differential phase shift, $\Delta\Phi = \Phi_H - \Phi_V$, due to the depolarization effect (Padullés et al., 2021).

The differential phase contribution along the propagation path is quantified by the specific differential phase, K_{dp}. Since the GNSS community generally uses length units (mm-shift/km-rain) rather than radians, K_{dp} is expressed in these units and multiplied by $\lambda/2\pi$. The equation for K_{dp} is:

$$K_{dp} = \frac{\lambda^2}{2\pi} \int \Re\{f_H(D) - f_V(D)\}N(D)dD \tag{1}$$

90   here, λ is the wavelength associated with GNSS; $\Re$ represents the real component; $f_H(D)$ and $f_V(D)$ are the forward scattering amplitudes, characterizing how GNSS waves scatter on hydrometeors for horizontal and vertical components, respectively; D is the drop's equivalent diameter; and $N(D)$ refers to the particle size distribution (PSD). The scattering amplitudes reflect the type and shape of each particle (e.g., liquid or solid).

The cumulative effect of hydrometeors along the ray path is then given by:

95 $$\Delta\Phi = \int_L K_{dp}(l)dl \tag{2}$$

In this expression, $\Delta\Phi$ is in units of mm, K_{dp} is in mm/unit-length and L represent the ray path length.

Calibrated PRO profiles from PAZ are available from May 2018 onward (Padullés et al., 2024). Each file corresponds to a PAZ observation and contains the vertical profile of the observable differential phase shift, $\Delta\Phi$, in units of length (mm) and relative to the tangential height of each PRO ray. Similarly, PRO data from Spire is available between May and October 2025,

100   and has undergone similar calibration as the PAZ data (Padullés et al., 2025a). As the PRO rays traverse the derived from PRO. This, in turn, provides valuable insightse from GPS to LEO, refractivity gradients cause bending, resulting in rays becoming tangent to the surface at their lowest point, termed the tangent point, h_t. The coordinates (latitude and longitude) for each PRO observation are based on this tangent point with $h_t = 4$ km. Though each ray relates to its tangential height, hydrometeors along its path contribute to the $\Delta\Phi$ value, regardless of altitude, since it is an integrated magnitude as we saw on Equation 2.

105   Additionally, the PRO files include the geographic positions (latitude, longitude, and altitude) of each ray path between GPS and PAZ, determined through ray-tracing. These locations are calculated and re-gridded so that only rays with a tangent height matching a regular grid between 0 and 20 km, with a vertical resolution of 0.1 km, are included. This approach ensures that ray trajectories align with the vertical resolution of $\Delta\Phi$ and represent the paths contributing to each $\Delta\Phi$ measurement. Each observation profile, whether from PAZ or Spire, has an identifier that we will refer to as "roid" from this point forward.

2.2   WRF simulations

The Weather Research and Forecasting-Advanced Research Weather (WRF-ARW) model was employed to simulate the ARs selected for the study. We have employed ERA5 reanalysis data for both initial and boundary conditions (Hersbach et al., 2020). To ensure the development of realistic atmospheric structures, the simulation was initialized 12 hours before the PRO observation time, following best practices for model spin-up (Skamarock et al., 2008). The simulations were performed with

115   two nested computational domains: a parent domain with a horizontal resolution of 15 km and a nested domain at 3 km resolution. A cumulus parameterization scheme was applied exclusively in the parent domain to account for unresolved convective processes (Skamarock et al., 2008). The model configuration featured 52 vertical layers, allowing for high-resolution vertical profiling, and a time step of 90 seconds for the integration.

4
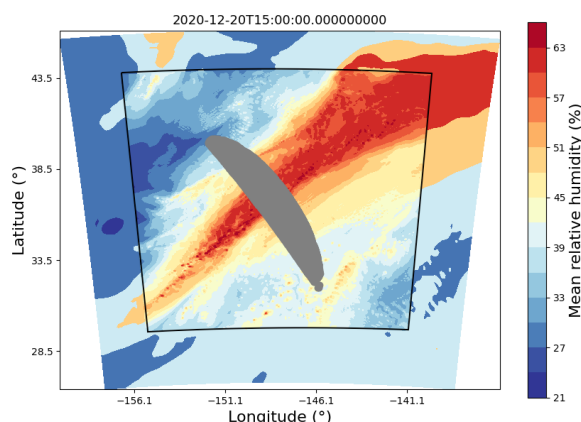
Figure 1. Mean relative humidity of an AR studied in this analysis, showing the two domains used in WRF. The grey area represents de 2D projection of the PRO rays below 20km.

Table 1. Physics schemes used in both domains for all the simulations performed with WRF.

	Domain 1 (15km)	Domain 2 (3km)
Cummulus	Kain-Fritsch	—
Shortwave and Longwave radiation	RRTMG	RRTMG
PBL	Yonsei University Scheme (YSU)	Yonsei University Scheme (YSU)
Land Surface	Unified Noah Land Surface Model	Unified Noah Land Surface Model
Surface Layer	MM5 Similarity Scheme	MM5 Similarity Scheme

An example of how the domains for the different ARs considered are defined can be seen in Figure 1. The simulations are structured such that the PRO observation point serves as the center of both domains, ensuring sufficient space to include all ray points below 20 km.

Four simulations were conducted for each AR, differing only in the microphysics schemes used: the Goddard scheme (Lin et al., 1983; Rutledge and Hobbs, 1984), the Thompson scheme (Thompson et al., 2008), the WSM6 scheme (Chen and Sun, 2002; Hong et al., 2004), and the Morrison two-moment scheme (Morrison and Pinto, 2005). This diverse selection of microphysics parameterizations enabled the evaluation of the sensitivity of AR simulations to different treatments of cloud microphysical processes. The rest of the schemes used are shown in Table 1.

5

For some of the simulations, instead of using the RRTMG schemes for shortwave and longwave radiation, the New Goddard Shortwave and Longwave Schemes were used due to certain errors that occurred in specific simulations.

The four different microphysics schemes employed in this study are Bulk Microphysics Schemes (BMS), which parameterize

130 precipitation particles as "bulk" quantities categorized into distinct hydrometeor classes, such as cloud water, rain, snow, ice, and others. In contrast, an alternative approach, known as Bin Microphysics Schemes, explicitly resolves the size distribution of cloud and precipitation particles by discretizing them into predefined "bins." Due to their computational efficiency, bulk schemes are widely utilized in operational weather forecasting and climate modeling.

The four schemes employed in the study predict six hydrometeor types: water vapor, cloud water, rain, snow, ice, and

135 graupel. The primary distinctions between these schemes lie in the specific microphysical processes and interactions governing the evolution of these hydrometeors. Below, we present a brief description of the schemes, highlighting some characteristics in comparison to other schemes or previous versions of the same.

– **Goddard**: This microphysics scheme is mainly based on Lin et al. (1983) with additional processes from Rutledge and Hobbs (1984). It has an option to choose whether hail or graupel is the third class of ice however, in this analysis the

140 Goddard 3ICE version with graupel is used. A new saturation technique (Tao et al., 1989) was introduced to prevent supersaturation or subsaturation at grid points that are clear or cloudy, respectively. Additionally, microphysical processes related to melting, evaporation, or sublimation are calculated based on the thermodynamic state, ensuring uniform treatment. Lastly, the total mass loss of any species will not exceed its available mass, ensuring a balanced water budget, (Tao et al., 2009; Skamarock et al., 2008).

145 – **WSM6**: This scheme is described in Hong and Lim (2006) and accounts for the same predicted variables as in WSM5 but includes graupel and its associated process described in Chen and Sun (2002). The ice-related microphysics are the ones proposed by Hong et al. (2004). From the WSM scheme series, the WSM6 is the most suitable for cloud-resolving grids (Skamarock et al., 2008).

– **Thompson**: Details of this scheme are in (Thompson et al., 2008). Unlike other bulk schemes, in this approach, snow size

150 distribution depends both on ice water content and temperature, and is represented as a gamma distribution, (Skamarock et al., 2008). Also, snow is considered non-spherical and its density varies inversely with diameter.

– **Morrison 2-moment**: The main difference between this scheme and the others is the two-moment part. One-moment schemes only predict the mixing ratios of the hydrometeor species; however, two-moment schemes also predict the number concentration of each hydrometeor. This scheme is based on Morrison et al. (2005) and Morrison and Pinto

155 (2006). It has also an option for choosing either graupel or hail, but in this analysis we have used the graupel option. The two-moment part allows for a more robust treatment of the size distribution enabling a better calculation of the microphysical process rates and evolution (Skamarock et al., 2008).
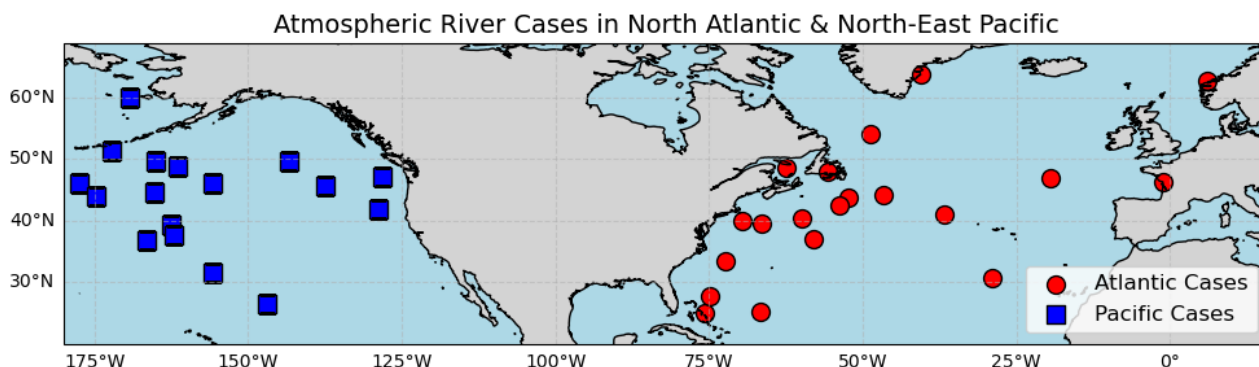
Figure 2. Coincidences between observation from PAZ and Spire with ARs. Each point represents the location of the PRO observation coincident with an AR.

For doing the different simulations we have selected different AR that are coincident in space and time with PAZ and Spire observations. In total we have 32 co-locations between ARs and PAZ and 5 between ARs and Spire. In Figure 2 we present the coincidences between ARs and PRO data from PAZ and Spire.

Likewise, the different ARs are classified according to their location. Of the 37 case studies we have, 20 correspond to north Atlantic ARs, and the other 17 to north-east Pacific ARs.

2.2.1 Evaluation of Atmospheric River Simulations

Before analyzing the impact of different schemes and particle habits on the observable $\Delta\Phi$ we perform a brief evaluation of the performance of the WRF simulations in reproducing the overall structure of ARs. This ensures that the simulations provide a realistic meteorological context before assessing microphysical sensitivities. For doing so, we present figures showing the Integrated Vapor Transport (IVT) and the acummulated total precipitation for each of the microphysics schemes, see Figure 3. In addition, the IVT from ERA5 reanalysis is shown and also the infrared temperature image, Figure 4, to provide an observational reference of the large-scale cloud structure of the AR.

The comparison between Figure 3 and Figure 4 indicates that all four microphysics schemes successfully capture the large-scale structure and intensity of the event, including the position, orientation of the moisture plume, and the magnitude of the IVT. This provides confidence in the realism of the simulated atmospheric features. In addition, the accumulated precipitation plots reinforce this finding, as they exhibit similar spatial patterns and plume alignment across all schemes. However, some differences can be observed in both the total amounts and the spatial distribution of precipitation. For instance, the Goddard and WSM6 schemes tend to produce more localized precipitation maxima, whereas Thompson and Morrison yield a broader, more distributed accumulation. Also, as will be discussed in the results section, differences between schemes become more pronounced when analyzing the vertical distribution and water content of the different hydrometeors (rain, snow, ice, and graupel), having a more direct impact on the simulated $\Delta\Phi$.
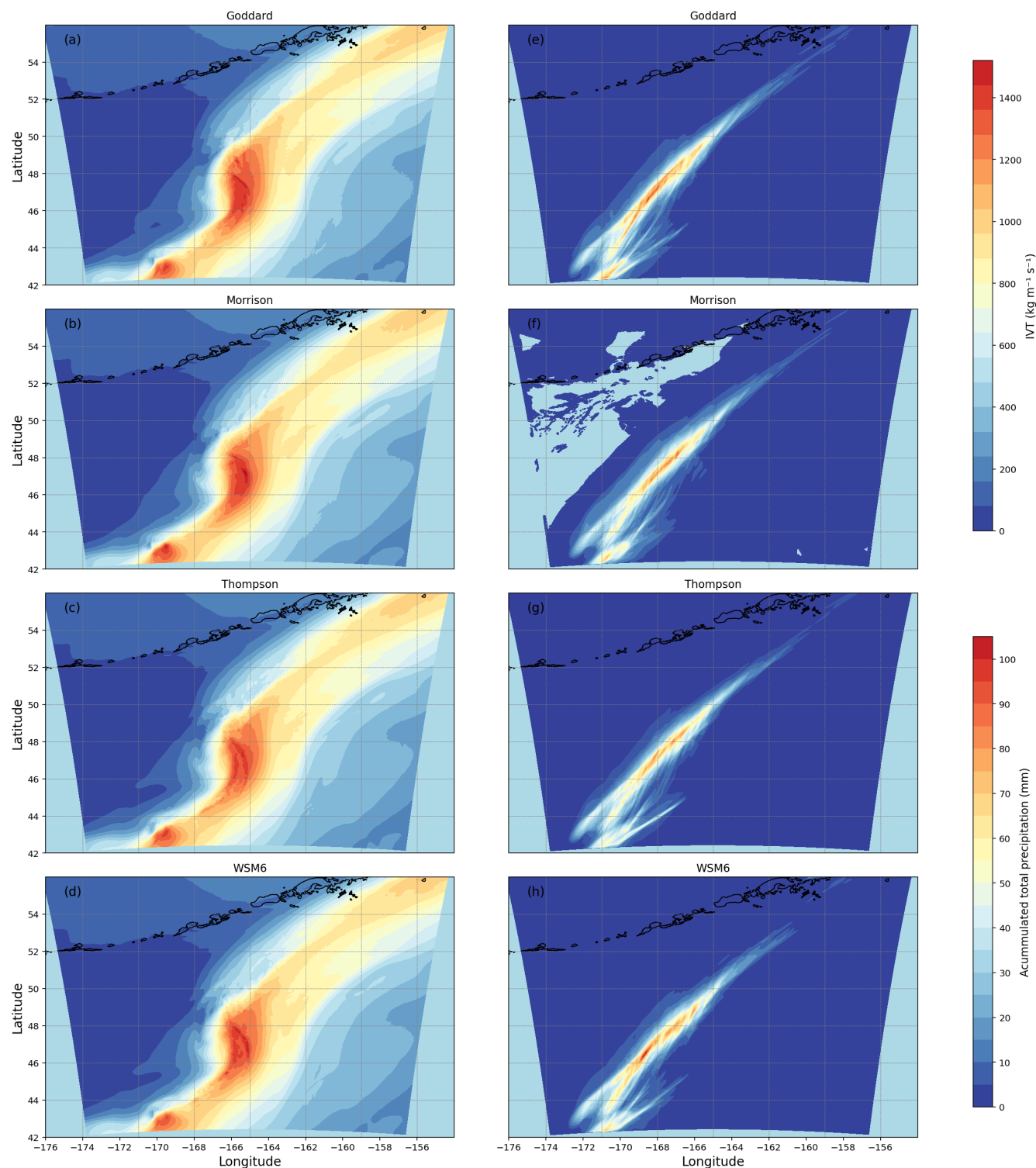
Figure 3. Panels (a), (b), (c) and (d) show the IVT from WRF for an specific AR depending on the microphysics scheme employed. Panels (e), (f), (g) and (h) show the accumulated total precipitation for the same schemes. The associated roid with this case is PAZ1.2018.239.03.26.G08.

8
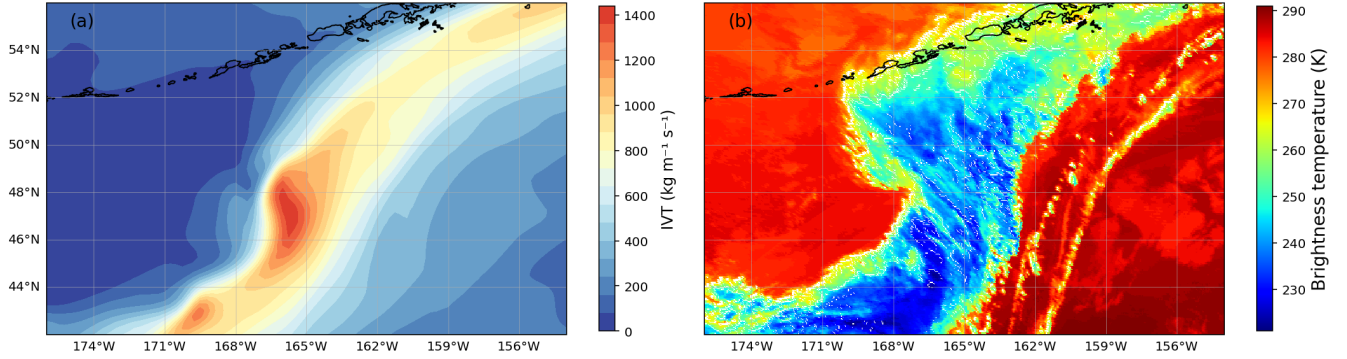
Figure 4. Panel (a) shows the IVT from ERA5 reanalysis and panel (b) the associated brightness temperature for the event associated with the observation PAZ1.2018.239.03.26.G08.

2.3 ΔΦ forward operator

In order to compare the vertical profiles of the $\Delta\Phi$ observed by PAZ and Spire with those simulated using the WRF model, a forward operator was developed. This operator computes the specific differential phase (K_{dp}) using water content derived from WRF simulations. For each habit in the ARTS database, a relationship between WC and K_{dp} has been computed (Padullés et al., 2025b), yielding the results shown here in Table 2. The parameters that relate WC with K_{dp} are defined here as x-parameters.

Then, the forward operator is defined as:

$$K_{dp} = K_{dp,rain} + x_{snow} \cdot WC_{snow} + x_{ice} \cdot WC_{ice} +$$
$$x_{graupel} \cdot WC_{graupel} \tag{3}$$

The simulated differential phase shift $\Delta\Phi_{sim}$ is then computed as:

$$\Delta\Phi_{sim} = \int K_{dp}dl = \int K_{dp,rain}dl + x_{snow} \cdot \int WC_{snow}dl +$$
$$x_{ice} \cdot \int WC_{ice}dl + x_{graupel} \cdot \int WC_{graupel}dl \tag{4}$$

In this formulation, each hydrometeor individually contributes to the total K_{dp}. For all hydrometeors except rain, the contribution is computed as the product of the x-parameter and the WC, derived from WRF. The water content is calculated based on the mixing ratios from WRF simulations using the following expression:

$$WC = q \cdot \frac{p}{R_{dry} \cdot T} \tag{5}$$

where q represents the mixing ratio, p is the pressure, $R_{dry} = 287.1 \times 10^{-3}$ kg m^{-3}K^{-1} is the specific gas constant for dry air, and T is the temperature. The contribution of rain ($K_{dp,rain}$) in Equation 3 is treated separately, as the ARTS database models rain as liquid spheres. It is computed using the following empirical relationship:

$$K_{dp,rain} = A \cdot WC_{rain}^B, \quad A = 0.13, \quad B = 1.314 \tag{6}$$

195

This formulation highlights the dependence of $K_{dp,rain}$ on the rainwater content, characterized by specific coefficients A and B, (Bringi and Chandrasekar, 2001).

Thus, the computed K_{dp} reflects not only the influence of the microphysical parameterizations used in WRF but also the specific particle habits assumed for the hydrometeors. However, this forward operator formulation has an inherent limitation:

200 it assumes a single particle habit per hydrometeor type, which may not fully capture the variability present in real atmospheric conditions. This assumption yields:

$$\Delta\Phi_{sim} = \Delta\Phi_{rain} + \sum_{sp} (x_{sp} \ \text{iWC}_{sp}) \tag{7}$$

where sp is the specie for the frozen hydrometeors (i.e. snow, ice, and graupel), and iWC is the integrated WC along the PRO ray paths corresponding to each specie.

205 Equation 7 allows for a detailed assessment of each hydrometeor's contribution (rain, snow, ice, and graupel) to the differential phase shift ($\Delta\Phi$). Each contribution depends on the WC derived from WRF simulations and the corresponding x-parameter, except for rain, which depends solely on WRF.

The methodology involves generating simulated $\Delta\Phi$ profiles for all possible combinations of water content and x-parameters. These combinations are determined independently of the particle habit. In other words, the x-parameters that multiply the dif-

210 ferent water contents can include all values, not just those corresponding to the specified hydrometeor habits. An optimization technique is then applied to identify the optimal x-parameter combinations for each microphysics scheme. Specifically, for each scheme, an inverse least-squares problem is solved to determine the x-parameters that minimize the discrepancy between the observed $\Delta\Phi_{obs}$ and the simulated $\Delta\Phi_{sim}$. The cost function associated with this optimization is defined as:

$$J(x) = (x - x_b)^T B^{-1}(x - x_b) + (y - H(x))^T R^{-1}(y - H(x)) \tag{8}$$

215 where x_b represents the initial estimate (background), y denotes the observation, $H(x)$ is the observation operator, and B and R are the covariance matrices of the background and observation, respectively. The final cost function, J, obtained for each observation is then divided by the number of points of the specific observation.

The x-parameters obtained through optimization do not necessarily match those presented in Table 2. To constrain the problem, specific bounds were set for each hydrometeor as an initial estimate: the upper limit for the x-parameter for all habits

220 is set to 0.758, that corresponds to the pristine ice plate fully horizontally oriented. The lower limit is set to 10^{-3}, that would

correspond to a particle that is nearly spherical. The final x-parameter is then associated with the particle habit that has the closest precomputed x-parameter from Table 2.

The background covariance matrix in Equation 8 is not considered in this study. The covariance matrix for observations is defined as follows:

$$R = \frac{1}{\sigma'^2} \tag{9}$$

where σ' is the standard error. For the dataset that has been used (e.g. Padullés et al., 2024), the σ' can be obtained using $\sigma' = SD/\sqrt{50}$, being SD the standard deviation of the differential phase obtained every 1 sec, that is, every 50 points.

Additionally, the standard deviations associated with the x-parameters were also calculated. Given that J is the cost function, the uncertainty associated with the x-parameters is given by the covariance matrix:

$$\mathbf{C}_x = \left(\mathbf{J}^\top \mathbf{J}\right)^{-1} \tag{10}$$

Then, the standard deviation of the x-parameters is:

$$\boldsymbol{\sigma}_x = \sqrt{\text{diag}(\mathbf{C}_x)} \tag{11}$$

3 Results and discussion

This section presents the results of the analysis and the corresponding discussion. The primary objectives are: (1) to study the contributions of hydrometeors to the WC and their influence on $\Delta\Phi_{sim}$; (2) to evaluate the performance of different microphysics schemes based on the GNSS-PRO observational data; (3) to analyze the impact of changing the particle habits on the $\Delta\Phi$; and (4) to investigate potential differences between ARs in the north Atlantic and north-east Pacific regions.

The results would inform us of which microphysics schemes and particle habits are most suitable to use in the simulation of ARs using WRF in particular, but also may provide insight to more general microphysics assumptions used in other models, such as operational forecasts.

### 3.1 Contribution of each hydrometeor to water content

First of all, we analyze the contribution of different hydrometeor species (i.e. rain, snow, ice and graupel), to the simulated differential phase shift, $\Delta\Phi_{sim}$. The analysis reveals that snow is the dominant contributor to the total water content, having the most significant influence on the differential phase shift. A correlation is observed between higher snow water content and an increased differential phase shift, underscoring the crucial role of snow in shaping the observed signal.

Among all the hydrometeors, snow consistently accounts for the largest fraction of total water content. Depending on the microphysics scheme and the specific AR case, either ice or rain are the second largest contribution. Figure 5 presents the

11

Table 2. Particle habits from ARTS used in the study, along with the x-parameters that are employed in the forward operator for calculating K_{dp}.

| Particle habit	x-parameter
HexColAggCrystal_Id21	0.017
LiuThickPlate_Id15	0.388
Rosette_Id36	0.017
HongBulletRosette_Id5	0.273
LiuSectorSnowflake_Id3	0.666
IconHail_Id30	0.008
HongBulletRosette_Id11	0.272
HexPlaAggCrystal_Id19	0.017
LiuLongColumn_Id14	0.425
LiuThinPlate_Id16	0.650
IconCloudIce_Id27	0.606
HexPlaAggCrystal_Id20	0.027
GemCloudIce_Id31	0.019
GemHail_Id34	0.003
HongBulletRosette_Id6	0.012
EvansSnowAgg_Id1	0.051
LiuShortColumn_Id13	0.269
HexColAggCrystal_Id18	0.017
HongAggregate_Id8	0.096
LiuBlockColumn_Id12	0.072
HexColAggCrystal_Id17	0.010
GemSnow_Id32	0.008
IconSnow_Id28	0.028
HongBulletRosette_Id2	0.086
HongBulletRosette_Id10	0.160
HongColumn_Id7	0.556
HongBulletRosette_Id4	0.016
HongPlate_Id9	0.758
HexColAggCrystal_Id22	0.025
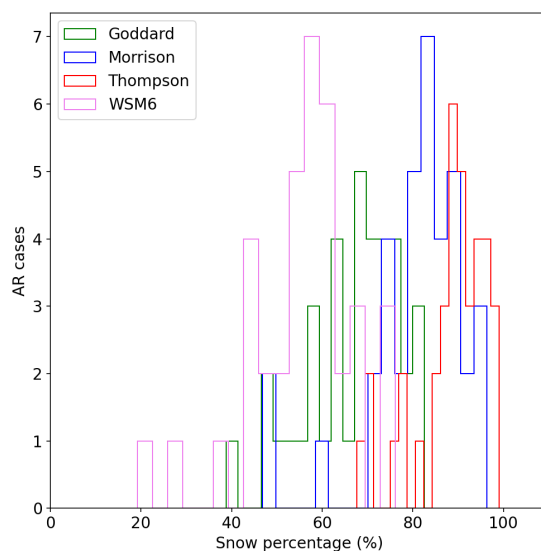
Figure 5. Percentage of snow water content from the total for each AR discerning between the different microphysics.

proportion of snow water content for each AR, categorized by microphysics scheme. This figure includes 37 observations per scheme, therefore showing the four simulations (changing only the microphysics scheme) of each AR case. In the subsequent analysis, we will look for the best solution among the different microphysics as the one that minimizes the cost function.

It is also worth noting that the contributions of ice and graupel exhibit greater variability across different microphysics schemes, whereas the contribution of rain remains relatively consistent for a given AR case. Additionally, in some cases, the agreement between $\Delta\Phi_{sim}$ and $\Delta\Phi_{obs}$ improved when the rain contribution was excluded. However, rain played a more significant role in cases where the maximum $\Delta\Phi$ was at lower altitudes, closer to the surface.

From Figure 5, it is evident that snow accounts for more than 40% of the total water content in most cases. The Thompson scheme predicts the highest snow water content, indicating a potential overestimation compared to other schemes. This overestimation is attributed to the scheme's generally low ice water content predictions, which result in a greater relative contribution from snow. In contrast, the Goddard and Morrison schemes exhibit a more balanced distribution of hydrometeors while still identifying snow as the dominant contributor. Notably, Morrison peaks at values similar to Thompson. Meanwhile, the WSM6 presents a broader distribution, including cases where the snow water content is lower ($20\% - 40\%$). Overall, WSM6 predicts the lowest snow percentages among the schemes, though snow remains the dominant hydrometeor.

To further explore this relationship, Figure 6 presents scatter plots illustrating the connection between vertically integrated iWC_{snow} and the vertically integrated $\Delta\Phi$ from PRO. To vertically integrate such quantities between two vertical levels (in this case, between 2 and 12km) yields a single value per observations, allowing a simpler comparison. Panels (a) and (b) focus
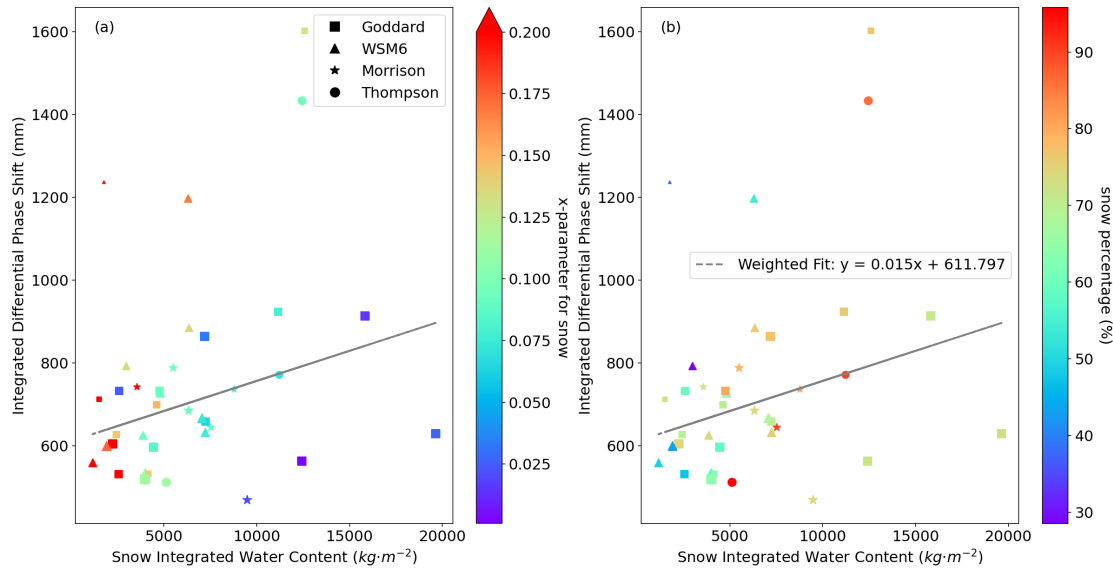
Figure 6. Scatter plots illustrating the relationship between integrated snow water content and integrated differential phase shift from PRO. Panel (a) presents points representing the best-performing microphysics scheme for each case, where each point is characterized by a unique marker shape corresponding to its microphysics scheme, a color scale representing the percentage of snow water content, and a size proportional to the cost function of the minimization process (larger points indicate lower costs). Panel (b) follows the same format but uses the color scale to represent the x-parameter for snow obtained through optimization.

on the best performing scheme (i.e., the one with the lowest cost function) for each AR case. Each data point corresponds to a specific microphysics scheme, with the color scale in panel (a) representing the optimized x-parameter for snow and in panel (b) indicating the percentage of snow water content relative to the total. The point size is proportional to the optimization cost function, with larger points representing lower cost values. The results confirm that higher snow water content generally leads to a greater differential phase shift. However, this trend is not uniformly evident due to differences in how each microphysics scheme estimates snow water content. For example, the Thompson scheme consistently predicts higher snow water content, reinforcing its tendency to overestimate the snow fraction.

Figure 6 further suggests that no universal relationship between $\Delta\Phi$ and snow water content, particularly given that the values shown are integrated over the vertical column. Variations along the rays must also be considered. Nevertheless, a dependence on x_{snow} and the percentage of snow water content can be observed in the relationship between these variables. This relationship appears to follow a slope of approximately $0.015 mm/(kg m^{-2})$. Additionally, the fitting process was performed using two parameters without forcing the trajectory through zero, recognizing that snow is not the only hydrometeor contributing to $\Delta\Phi$.
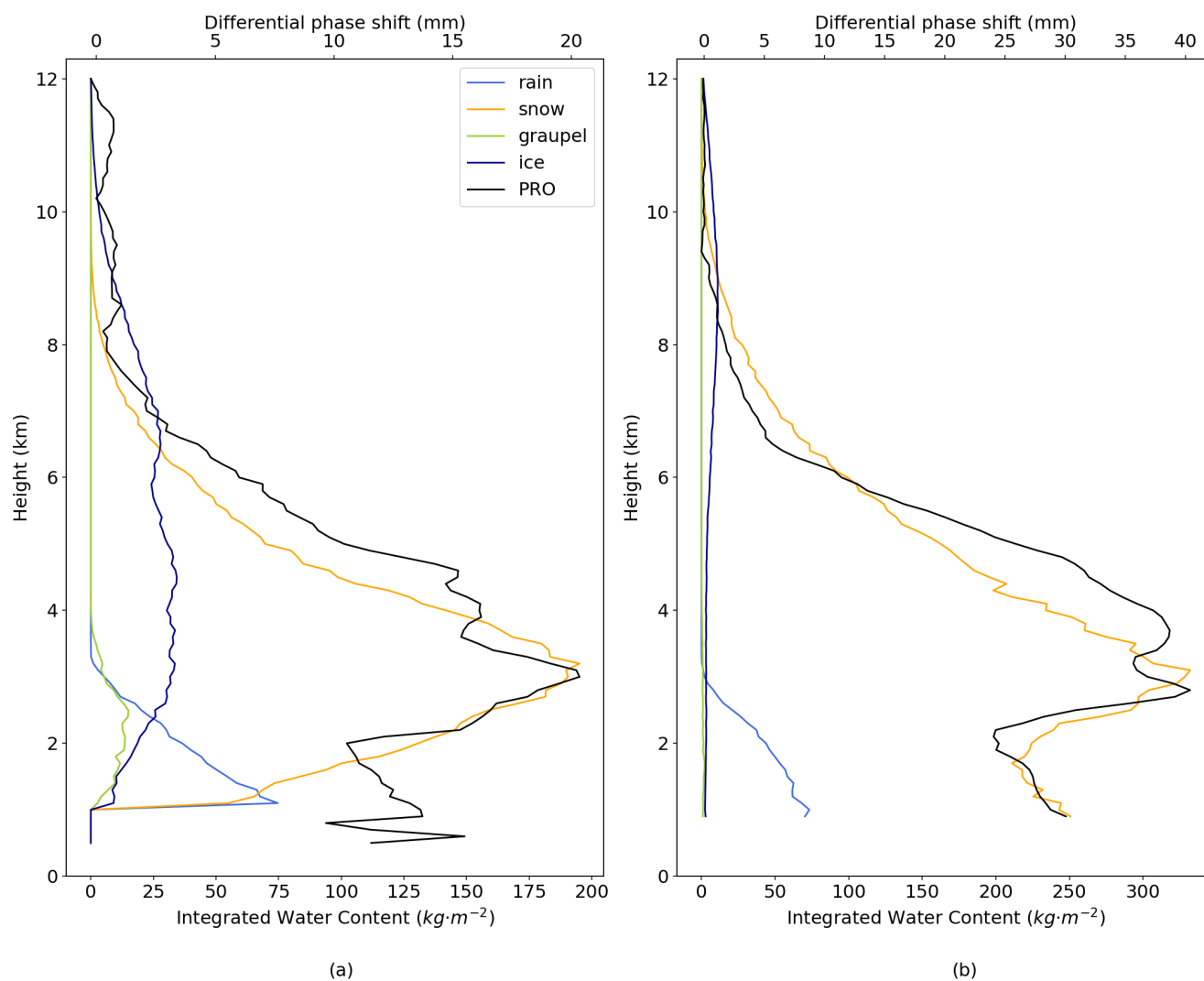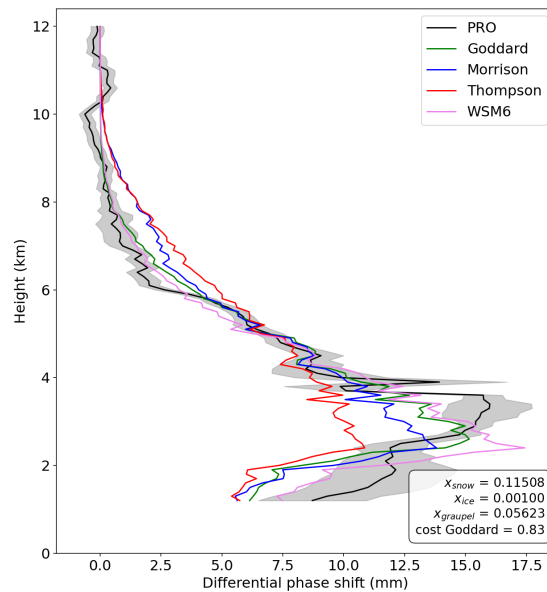
Figure 7. Vertical profiles of the differential phase shift (top x-axis) obtained from PAZ and the integrated water content (bottom x-axis) from WRF for the different hydrometeors. The microphysics schemes used were Goddard (a) for the observation with roid PAZ1.2019.142.10.32.G02 and Morrison (b) for the observation with roid PAZ1.2023.038.10.59.G19 scheme.

To further illustrate the findings discussed above, we present in Figure 7 the following profiles for two different observations. These profiles display the $\Delta\Phi$ from PRO alongside the integrated water content profiles for each hydrometeor, considering a specific microphysics scheme. It is clearly observed that snow contributes the most and closely follows the shape of the observed $\Delta\Phi$.

3.2 Discerning between different microphysics

Even though the minimization of J is performed jointly for both the microphysics scheme and x-parameter, in this section we focus exclusively on the influence of the microphysics scheme, regardless of the x-parameter. This preliminary analysis aims to identify the microphysics schemes that most accurately replicate the GNSS-PRO observations.

Figure 8. Vertical profiles of the differential phase shift obtained from GNSS-PRO and from the different microphysics of WRF. We also present the standard deviation of $\Delta\Phi$ from PRO in grey. The x-parameters optimized and the cost function associated with the best microphysics (Goddard) are presented in the legend. The roid of the observation is PAZ1.2021.034.10.07.G08.

Figure 8 presents an example of a profile $\Delta\Phi_{sim}$ obtained from the four different microphysics schemes along with the corresponding observation of PRO. In this particular case, the profile obtained using the Goddard microphysics scheme exhibits a better fit to the observed data. The x-parameters resulting from the optimization for each hydrometeor, along with the corresponding cost function value, are displayed within the same figure.

16
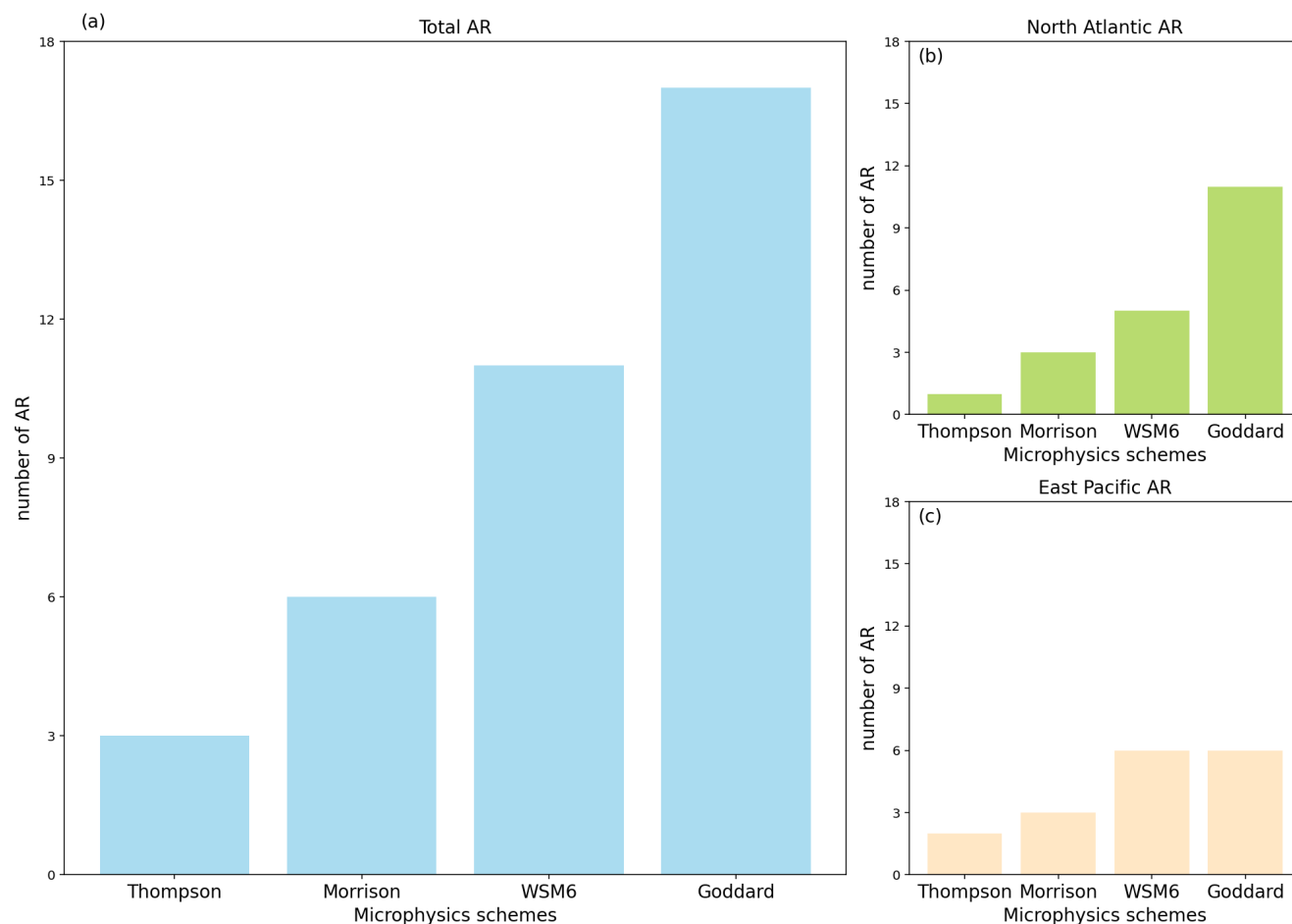
Figure 9. Histogram showing the number of AR that perform best with each microphysics. The performance of each scheme is evaluated using the cost function J resulted from the optimization.

The general results primarily depend on how each microphysics scheme simulates snow, including both its quantity and vertical distribution. Even slight variations in the snow's position can lead to differences in the results. However, the large-scale characteristics of atmospheric rivers tend to mitigate these effects.

Figure 9 presents a histogram summarizing the microphysics schemes that achieved the best agreement with PRO observations. For each case, the optimal scheme is identified based on the lowest cost function, J (see Equation 8). The results indicate that the Goddard scheme consistently outperforms the others, followed by WSM6.

Further analysis reveals that the Thompson scheme often underrepresents the ice in $\Delta\Phi_{sim}$, occasionally omitting it entirely. Meanwhile, the WSM6 scheme predicts the lowest snow water content and appears to overestimate graupel, potentially contributing to discrepancies with PRO observations. Differences in the treatment of ice also distinguish the Morrison and Goddard schemes, with Morrison predicting lower ice content concentrated at higher altitudes. Regarding graupel, no clear

trend is observed across the different schemes. However, differences among the schemes are evident when analyzed across

300   multiple AR cases.

In terms of snow, which is the dominant hydrometeor in all schemes, no clear trends are identified across different microphysics schemes. For rain, the contributions remain relatively consistent across all cases, suggesting that variations in performance are primarily driven by differences in the treatment of frozen hydrometeors.

3.3   Sensitivity to different particle habits
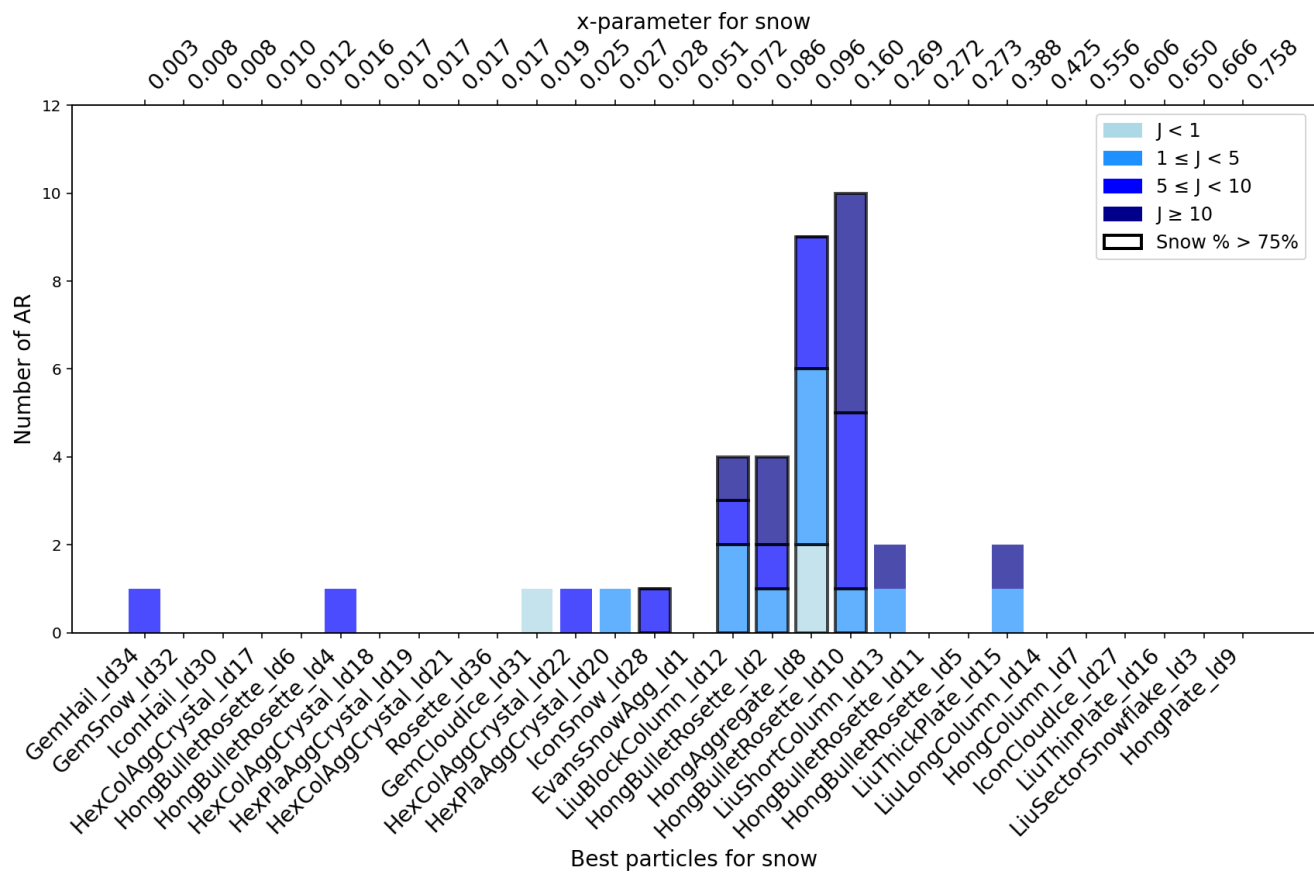
Figure 10. Histogram showing the particle habits for snow corresponding with the best case resulted from the optimization, this means, one habit per AR. We also show the associated x-parameter to each particle.

305   Building on the findings from the previous sections, namely that snow is the dominant contributor and that the Goddard microphysics scheme generally yields the best results, this section explores which particle habits provide the best agreement with observations.

The parameter ranges considered during the optimization are the same for the three species that are considered here (snow, ice, and graupel), and must lay within [0.001,0.758]. These values are based on the maximum values obtained from the simu-
310   lations of the particle shapes from the ARTS database, and setting 10^{-3} as a minimum value, equivalent to a nearly spherical habit. However, these values do not account for particle orientation, such as the distribution of canting angles. If canting information is included, habits with initially higher x-parameter may exhibit lower values, as the canting angle reduces the overall x-parameter (Padullés et al., 2025b).

Figure 10 presents a histogram of the snow particle habits obtained from the optimization process, considering only those
315   associated with the best performing microphysics scheme for each AR. The results indicate that the habits most closely aligning with observations are $HongBulletRosette\_Id10$ and $HongAggregate\_Id8$, which correspond to a bullet rosette and a snow aggregate, respectively. Furthermore, the optimized results generally cluster around $x_{snow} = 0.1mm/kg\,m^{-2}$.

In the same Figure 10, we distinguish cases where the snow water content percentage exceeds 75%. As shown, these cases are associated with x_{snow} values ranging approximately from 0.05 to 0.16$mm/(kg\,m^{-2})$. In addition, we differentiate cases
320   based on the value of the cost function. Although the most frequently occurring particle habits are associated with higher cost function values, certain outlier habits also correspond to high cost function values, suggesting a more complex relationship between habit selection and optimization performance.

The predominance of snow aggregates and bullet rosettes as the optimal habit aligns with physical expectations, as these particles exhibit complex and irregular structures. The loosely bound individual crystals within aggregates influence their
325   scattering properties. In contrast, cases where snow was classified as plate-like structures showed a significant overestimation of snow contribution. This discrepancy likely arises from the highly directional scattering behavior of snow plates, which results from their compact and well-defined crystalline structures, leading to an overestimation in observed values. These findings underscore the importance of accurate microphysical parameterization in numerical models to properly represent snowfall characteristics.

330   Similarly, histograms analogous to Figure 10 were generated for graupel and ice (not shown). In general, the x-parameter for ice and graupel have a much lower value than that of snow, in agreement with snow being the largest contributor to $\Delta\Phi$.

Figure 11 presents the summary of the values of the x-parameters corresponding to the best-performing microphysics scheme for each AR, for snow, ice, and graupel. The first relevant thing to note is that the optimized values for ice and graupel often lay over the lower limit (the allowed range of x-parameters values is shown with a gray shaded area). Furthermore, the large
335   error bars for these species indicate that they have a minor contribution to $\Delta\Phi$, since the minimization does not depend much on their value. Overall, the smallest error bars are obtained for snow, and its x-parameter values indeed appear to follow a more consistent trend around approximately $x = 0.1mm/kg\,m^{-2}$ (as seen in Figure 10). Additionally, Figure A1 in the Appendix presents a 2D plot of the cost function as a function of the x-parameters for snow and ice. Each plot corresponds to a specific observation, with the case PAZ1.2018.234.06.45.G06, Figure A1 (a), representing one where the error bars in Figure 11 are
340   relatively small, and PAZ1.2022.122.01.17.G25, Figure A1, representing a case with substantially larger error bars. In both plots, the x-parameter for graupel was set to the minimum value obtained for each respective case. This figure illustrates the distribution of the cost function for one scenario in which the parameter values significantly influence the final agreement,
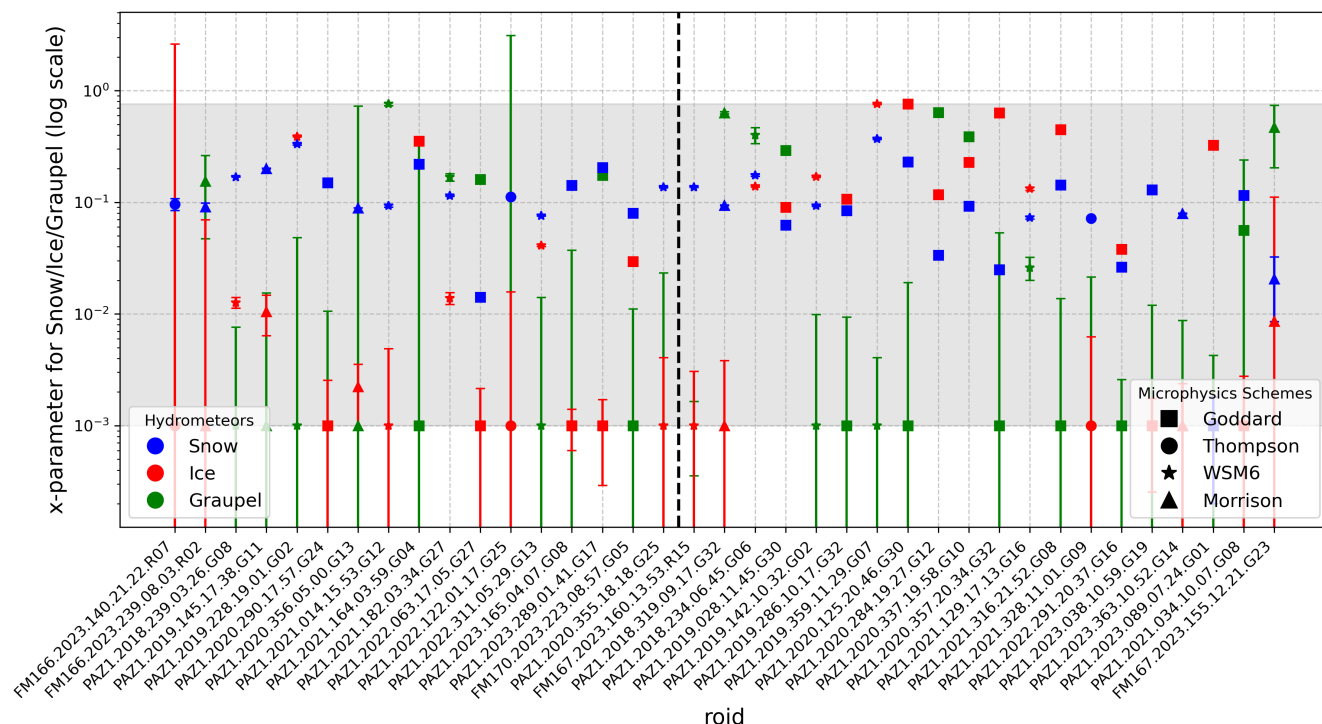
Figure 11. Scatter plot showing the different values of the x-parameters for the best-performing microphysics scheme for each AR case. Additionally, error bars are presented for each value, along with the optimization range of the hydrometeors (shaded colored area). The y-axis is in logarithmic scale. The dashed line represents a division between the regions of each observation: those on the left correspond to the Pacific, while those on the right correspond to the Atlantic.

compared to a case where their relevance is diminished. Notably, the contours for PAZ1.2018.234.06.45.G06 appear more defined around specific x-parameter values, whereas the contours in the other case are more diffuse, indicating less sensitivity to parameter selection.

Additionally, we also present a figure in the Appendix showing the best x-parameters for snow as a function of the microphysics scheme (Figure B1). In general, we observe that the same trend holds across all microphysics schemes, and the most frequent particle habits are the same as those in Figure 10. With the exception of Thompson where the $HongAggregate\_Id8$ outstands slightly the others, and WSM6 where $HongBulletRosette\_Id10$ overcomes the rest.

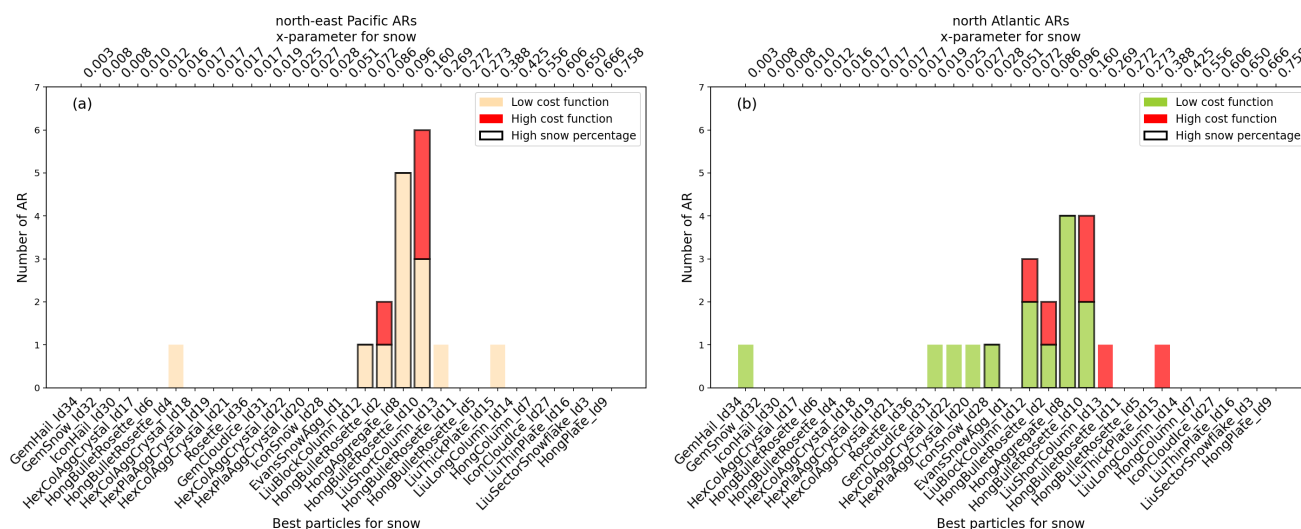## 3.4 ARs over the North Atlantic and East Pacific

Given that ARs occurring in the Atlantic and Pacific originate from distinct moisture sources and are exposed to varying atmospheric conditions, it can be hypothesized that there might be differences in the vertical distribution of hydrometeors.

In this section, after analyzing the different cases and reviewing the results from the analysis already discussed, we will examine whether the location of the AR influences the conclusions we can draw. In total, we have 37 ARs, with 20 located in

355   the north Atlantic and 17 in the north-east Pacific.

From what concerns to the microphysics schemes, Figure 9 (b) and (c) shows the Goddard scheme is the most frequently identified as the best performing scheme across all AR, suggesting that it provides the most consistent agreement with PRO. The WSM6 scheme also performs well but is less dominant than Goddard. The Morrison and Thompson schemes appear less frequently, indicating that they may not be as effective in reproducing the observed conditions. It seems that the general trend

360   observed for the 37 ARs is the same as in the individual cases of the Atlantic and the Pacific, but for the Pacific cases we can highlight the same good performance of Goddard and WSM6, fact that is not as remarkable as in the Atlantic cases.

Another distinction emerges in Figure 11 when comparing Atlantic and Pacific AR. As shown by the dashed line in the same figure, which separates Pacific (left) from Atlantic (right) AR. The particle habits for ice in the Atlantic AR tend to have higher x-parameters compared to those from the Pacific, suggesting that ice is given a greater contribution in the Atlantic cases. Also,

365   the error bars for the ice are larger for the Pacific cases compared to the Atlantic ones. Above all, for graupel, same happens for the error bars in comparison with the Atlantic. This suggests that in certain Pacific cases, the selection of the particle for graupel and ice does not play an important role.

Figure 12. Histograms showing the best particle habits for the different AR as sin Figure 10 but discerning between those AR from the Pacific (a) and from the Atlantic (b).

Regarding the type of particle habits, we present the following histograms in Figure 12. From this Figure 12, no clear trend is observed for AR located in the Atlantic. However, $LiuBlockCOlumn\_Id12$ and $HongBulletRosette\_Id10$ are the two most

370 frequently particle habits obtained. In contrast, for ARs in the Pacific, the dominant habits are again $HongAggregate\_Id8$ and $HongBulletRosette\_Id10$.

4   Conclusions

This study demonstrates that GNSS-PRO is an effective tool for distinguishing between different microphysics parameterizations and various particle habits in the modeling of ARs. The results obtained from WRF and ARTS simulations show strong

375 agreement with PRO observations, particularly in capturing the differential phase shift, $\Delta\Phi_{sim}$. Among the hydrometeors considered, snow emerges as the dominant contributor to $\Delta\Phi_{sim}$, underscoring its critical role in shaping the observed signal. The Goddard microphysics scheme consistently provides the best performance across cases, likely due to its more balanced representation of hydrometeors.

The effectiveness of each microphysics scheme varies depending on the specific AR analyzed; however, certain trends re-

380 main consistent. The Thompson scheme tends to underestimate ice concentrations while overestimating snow water content, which negatively impacts its agreement with GNSS-PRO. Conversely, the Goddard and WSM6 schemes yield the highest ice concentrations, while the Morrison scheme generally predicts lower ice content. These differences highlight the significant influence of microphysics parameterizations on model accuracy and their implications for interpreting observational datasets. The incorporation of GNSS-PRO observations into microphysics development could enhance the refinement of parameterizations,

385 particularly for snow and other frozen hydrometeors.

Furthermore, while ice and graupel exhibit varying contributions depending on the microphysics scheme, the role of rain remains relatively consistent across different schemes for the same AR. In most cases, including or excluding rain does not significantly impact the agreement between $\Delta\Phi_{sim}$ and $\Delta\Phi_{obs}$, except when the maximum $\Delta\Phi$ occurs at lower altitudes closer to the surface. This behavior aligns with expectations, as rain is a more spatially variable phenomenon compared to

390 frozen hydrometeors.

Regarding the x-parameter for snow we have seen that even though there is variability among cases the results tend to systematically group around 0.05-0.2. This corresponds to habits like aggregates, columns, and bullet rosettes, and discards the systematic presence of horizontally oriented plate-like habits. Likewise, the presence of orientable shaped habits is required in order to explain the observations, and therefore we can discard snow being contributed by spheres or habits that are totally

395 randomly oriented.

The analysis also reveals some differences between Atlantic and Pacific ARs in terms of particle habits, while microphysics schemes do not seem to play a significant role in distinguishing between them. Interestingly, for Atlantic ARs, the best-performing ice habits tend to be more distributed than those in Pacific ARs, suggesting a greater relative contribution of ice in these cases.

400 Overall, these findings underscore the importance of selecting appropriate microphysics schemes to accurately represent snow processes and the necessity for further research into the sensitivity of these schemes to observational and modeling

uncertainties. The results also highlight the need for additional validation using independent datasets to improve the reliability of hydrometeor property retrievals.

As for future work, it would be interesting to consider additional aspects of particle habits when analyzing the agreement with PRO observations. Factors such as the canting angle or the use of different habits for the same hydrometeor depending on variables like temperature could provide further insights.

References

Bringi, V. N. and Chandrasekar, V.: Polarimetric Doppler weather radar: principles and applications, Cambridge university press, 2001.

420   Cardellach, E., Tomás, S., Oliveras, S., Padullés, R., Rius, A., de la Torre-Juárez, M., Turk, F. J., Ao, C. O., Kursinski, E. R., Schreiner, B., Ector, D., and Cucurull, L.: Sensitivity of PAZ LEO Polarimetric GNSS Radio-Occultation Experiment to Precipitation Events, IEEE Transactions on Geoscience and Remote Sensing, 53, 190–206, https://doi.org/10.1109/TGRS.2014.2320309, 2015.

Cardellach, E., Oliveras, S., Rius, A., Tomás, S., Ao, C., Franklin, G. W., Iijima, B. A., Kuang, D., Meehan, T. K., Padullés, R., de la Torre Juárez, M., Turk, F., Hunt, D. C., Schreiner, W. S., Sokolovskiy, S. V., Hove, T. V., Weiss, J. P., Yoon, Y., Zeng, Z., Clapp, J., Xia-

425   Serafino, W., and Cerezo, F.: Sensing Heavy Precipitation With GNSS Polarimetric Radio Occultations, Geophysical Research Letters, 2019.

Chen, S. H. and Sun, W. Y.: A one-dimensional time dependent cloud model, Journal of the Meteorological Society of Japan, 2002.

Geer, A. J., Bauer, P., Lonitz, K., Barlakas, V., Eriksson, P., Mendrok, J., Doherty, A., Hocking, J., and Chambon, P.: Bulk hydrometeor optical properties for microwave and sub-millimetre radiative transfer in RTTOV-SCATT v13. 0, Geoscientific Model Development, 14,

430   7497–7526, 2021.

Haase, J. S., Murphy, M. J., Cao, B., Ralph, F. M., Zheng, M., and Delle Monache, L.: Multi-GNSS Airborne Radio Occultation Observations as a Complement to Dropsondes in Atmospheric River Reconnaissance, Journal of Geophysical Research: Atmospheres, 126, 1–24, https://doi.org/10.1029/2021JD034865, 2021.

Healy, S. B., Jupp, A. M., and Marquardt, C.: Forecast impact experiment with GPS radio occultation measurements, Geophysical Research

435   Letters, 2005.

Hersbach, H., Bell, B., Berrisford, P., Hirahara, S., Horányi, A., Muñoz-Sabater, J., Nicolas, J., Peubey, C., Radu, R., Schepers, D., Simmons, A., Soci, C., Abdalla, S., Abellan, X., Balsamo, G., Bechtold, P., Biavati, G., Bidlot, J., Bonavita, M., Chiara, G. D., Dahlgren, P., Dee, D., Diamantakis, M., Dragani, R., Flemming, J., Forbes, R., Fuentes, M., Geer, A., Haimberger, L., Healy, S., Hogan, R. J., Hólm, E., Janisková, M., Keeley, S., Laloyaux, P., Lopez, P., Lupu, C., Radnoti, G., de Rosnay, P., Rozum, I., Vamborg, F., Villaume, S., and Thépaut,

440   J.-N.: The ERA5 global reanalysis, Quarterly Journal of the Royal Meteorological Society, 2020.

Hong, S. Y. and Lim, J. O. J.: The WRF single-moment 6-class microphysics scheme, Asia-Pacific Journal of Atmospheric Sciences, 2006.

Hong, S. Y., Dudhia, J., and Chen, S. H.: A revised approach to ice microphysical processes for the bulk parameterization of clouds and precipitation, Monthly Weather Review, 2004.

Kursinski, E. R., Hajj, G. A., Schofield, J. T., Linfield, R. P., and Hardy, K. R.: Observing Earth's atmposhere with radio occultation mea-

445   surements using the Global Positioning System, Journal of Geophysical Research: Atmospheres, 1997.

Lin, Y. L., Farley, R. D., and Orville, H. D.: Bulk parameterization of the snow field in a cloud model, Journal of Applied Meteorology and climatology, 1983.

Morrison, H. and Pinto, J. O.: Mesoscale modeling of spring-time arctic mixed-phase clouds using a new two-moment bulk microphysics scheme, Journal of the Atmospheric Society, 2005.

450   Morrison, H. and Pinto, J. O.: Intercomparison of bulk cloud microphysics schemes in mesoscale simulations of springtime Arctic mixed-phase stratiform clouds, Monthly Weather Review, 2006.

Morrison, H., Curry, J. A., and Khvorostyanov, V. I.: A New Double-Moment Microphysics Parameterization for Application in Cloud and Climate Models. Part I: Description, Journal of the Atmospheric Sciences, 2005.

Murphy, M. J. and Haase, J. S.: Evaluation of GNSS Radio Occultation Profiles in the Vicinity of Atmospheric Rivers, Atmosphere, 13,
    1495, https://doi.org/10.3390/atmos13091495, 2022.

Murphy, M. J., Haase, J. S., Padullés, R., Chen, S. H., and Morris, M. A.: The potential for discriminating microphysical pro-
    cesses in numerical weather forecasts using airborne polarimetric radio occultations, Remote Sensing, 11 (19), U2048–U2072,
    https://doi.org/10.3390/rs11192268, 2019.

Padullés, R., Ao, C., Turk, F., de la Torre Juárez, M., Iijima, B., Wang, K. N., and Cardellach, E.: Calibration and validation of the Polarimetric
    Radio Occultation and Heavy Precipitation experiment aboard the PAZ satellite, Atmospheric Measurement Techniques, 2020.

Padullés, R., Cardellach, E., Turk, F., Ao, C., de la Torre Juárez, M., Gong, J., and Wu, D. L.: Sensing Horizontally Oriented Frozen Particles
    With Polarimetric Radio Occultations Aboard PAZ: Validation Using GMI Coincident Observations and Cloudsat a Priori Information,
    IEEE Transactions on Geoscience and Remote Sensing, 2021.

Padullés, R., Cardellach, E., and Turk, F.: On the global relationship between polarimetric radio occultation differential phase shift and ice
    water content, Atmospheric Chemistry and Physics, 2023.

Padullés, R., Cardellach, E., and Oliveras, S.: resPrf [Dataset], https://doi.org/10.20350/digitalCSIC/16137, 2024.

Padullés, R., Cardellach, E., Paz, A., and Burger, T.: Initial Polarimetric Radio Occultation Results from Spire's Nanosatellite Constellation:
    Independent assessment and potential applications, Bulletin of the American Meteorological Society, https://doi.org/10.1175/BAMS-D-
    23-0322.1, 2025a.

Padullés, R., Cardellach, E., Paz, A., and Turk, F. J.: Polarimetric Radio Occultation Forward Scattering Sensitivity to Hydrometeor Habit,
    submitted to Geophysical Research Letters, https://doi.org/XX.XXXXX/XXXXXXXX, 2025b.

Padullés, R., Cardellach, E., Paz, A., and Turk, F. J.: Scattering amplitude matrix co-polar components for GNSS Polarimetric Radio Occul-
    tations observation geometry [Dataset], https://doi.org/10.20350/digitalCSIC/17140, 2025c.

Paz, A., Padullés, R., and Cardellach, E.: Evaluating the Polarimetric Radio Occultation Technique Using Nexrad Weather Radars, Remote
    Sensing, 2024.

Rutledge, S. A. and Hobbs, P. V.: The mesoscale and microscale structure and organization of clouds and precipitation in midlatitude cyclone.
    Part XII: A diagnostic modeling study of precipitation development in narrow cold-frontal rainbands, Journal of the Atmospheric Sciences,
    1984.

Skamarock, W. C., Klemp, J. B., Dudhia, J., Gill, D. O., Barker, D. M., Duda, M. G., Huang, X.-Y., Wang, W., and Powers, J. G.: A description
    of the advanced research WRF version 3, NCAR technical note, 2008.

Skamarock, W. C., Klemp, J. B., Dudhia, J., Gill, D. O., Zhiquan, L., Berner, J., Wang, W., Powers, J. G., Duda, M. G., Barker, D. M., and
    Huang, X.-Y.: A Description of the Advanced Research WRF Model Version 4.3, NCAR Technical Note NCAR/TN-556+STR, p. 145,
    https://doi.org/10.5065/1dfh-6p97, 2019.

Talpe, M., Nguyen, V., and Tomás, S.: Initial Polarimetric Radio Occultation Results from Spire's Nanosatellite Constellation: Satellite
    Payload, Collection and Calibration, Bulletin of the American Meteorological Society, https://doi.org/10.1175/BAMS-D-23-0314.1, 2025.

Tao, W. K., Simpson, J., and McCumber, M.: An ice-water saturation adjustment, Monthly Weather Review, 1989.

Tao, W. K., Shi, J. J., Chen, S. S., Lang, S., Hong, S. Y., Thompson, G., Peters-Lidard, C., Hou, A., Braun, S., and Simpson, J.: Studying
    precipitation processes in WRF with Goddard bulk microphysics in comparison with other microphysical schemes, 2009.

Thompson, G., Field, P. R., Rasmussen, R. M., and Hall, W. D.: Explicit forecasts of winter precipitation using an improved bulk microphysics
    scheme. Part II: Implementation of a new snow parameterization, Monthly Weather Review, 2008.

Turk, F., Padullés, R., Cardellach, E., Ao, C., Wang, K.-N., Morabito, D. D., de la Torre Juárez, M., Oyola, M., Hristova-Veleva, S., and Neelin, J. D.: Interpretation of the Precipitation Structure Contained in Polarimetric Radio Occultation Profiles Using Passive Microwave Satellite Observations, Journal of Atmospheric and Oceanic Technology, 2021.

Appendix A: Appendix1

495 Figure A1 complements the earlier Figure 11 by presenting a two-dimensional sensitivity map of the cost function with respect to the x-parameters of snow and ice, where the graupel values are fixed. This visualization helps us understand the interdependency between these two hydrometeors in terms of their influence on the differential phase shift.

Figure A1 (a), shows an observation (PAZ1.2018.234.06.45.G06) corresponding to an optimization result with small error bars, indicating high confidence in the measured differential phase shift. The cost function map for this case is more structured, with a well-defined minimum region. This suggests that the optimization process is better constrained, and that we can identify a relatively precise combination of x-parameters for snow and ice that provides the best match to the observed data. The contours guide us to this optimal region, typically centered around x-parameters for snow close to 0.1.

In contrast, Figure A1 (b) shows an observation (PAZ1.2022.122.01.17.G25) with very large error bars, where the uncertainty in the measurement significantly reduces our ability to constrain the optimal solution. The cost function is relatively flat across a broader region, with the minimum being less defined and spread over a larger range of x-parameters. Multiple combinations of snow and ice x-parameters yield similar low cost values, making it harder to select a dominant particle habit.
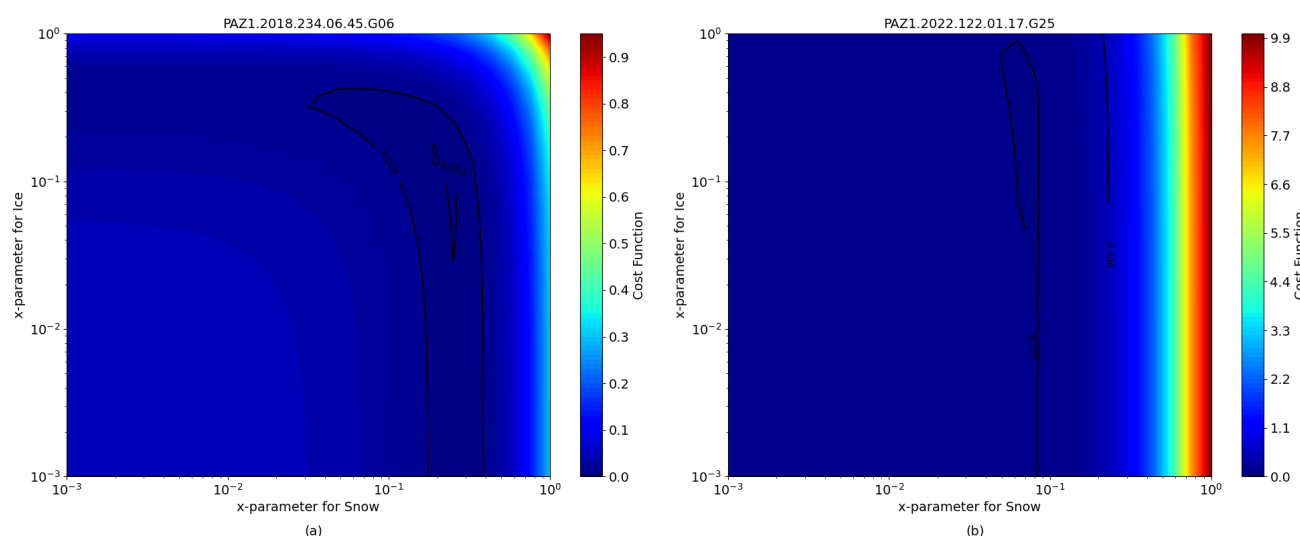
Figure A1. Two-dimensional plot showing the cost function values associated with two cases depending on the values of the x-parameters for snow and ice. The x-parameter values associated with graupel are constant and correspond to the minimum value.

Appendix B: Appendix2

From the analysis of particle habits, we also present Figure B1, which shows the optimal x-parameters for snow depending on the microphysics. As previously discussed, the two most frequent particle habits, $HongAggregate\_Id8$ and $HongBulletRosette\_Id10$, are clearly reflected in these histograms.

Notably, for the Thompson microphysics scheme, all ARs exhibit a snow water content percentage above 75%, as indicated by the black border bars. This suggests that the Thompson scheme systematically simulates a dominance of snow in these events, regardless of the chosen particle habit. In this scheme, we can also see a broader presence of higher cost function values, possibly indicating challenges in fitting PRO observations despite high snow representation. For Goddard and WSM6, both show a group of optimal x-parameters around the 0.08–0.1 range, again pointing to aggregates and bullet rosettes as the most representative snow habits. Whereas for Morrison, although having a broader distribution, we still observe a concentration in this same range, but with slightly more cases where the cost function exceeds 10 (red bars).

Overall, this figure supports the idea that aggregates and bullet rosettes consistently yield better agreement with PRO, and that x-parameters around $0.1(mm/kg \cdot m^{-2})$ are particularly effective across various schemes. It also highlights how the microphysics schemes differ not just in accuracy, but in their hydrometeor composition trends.

27
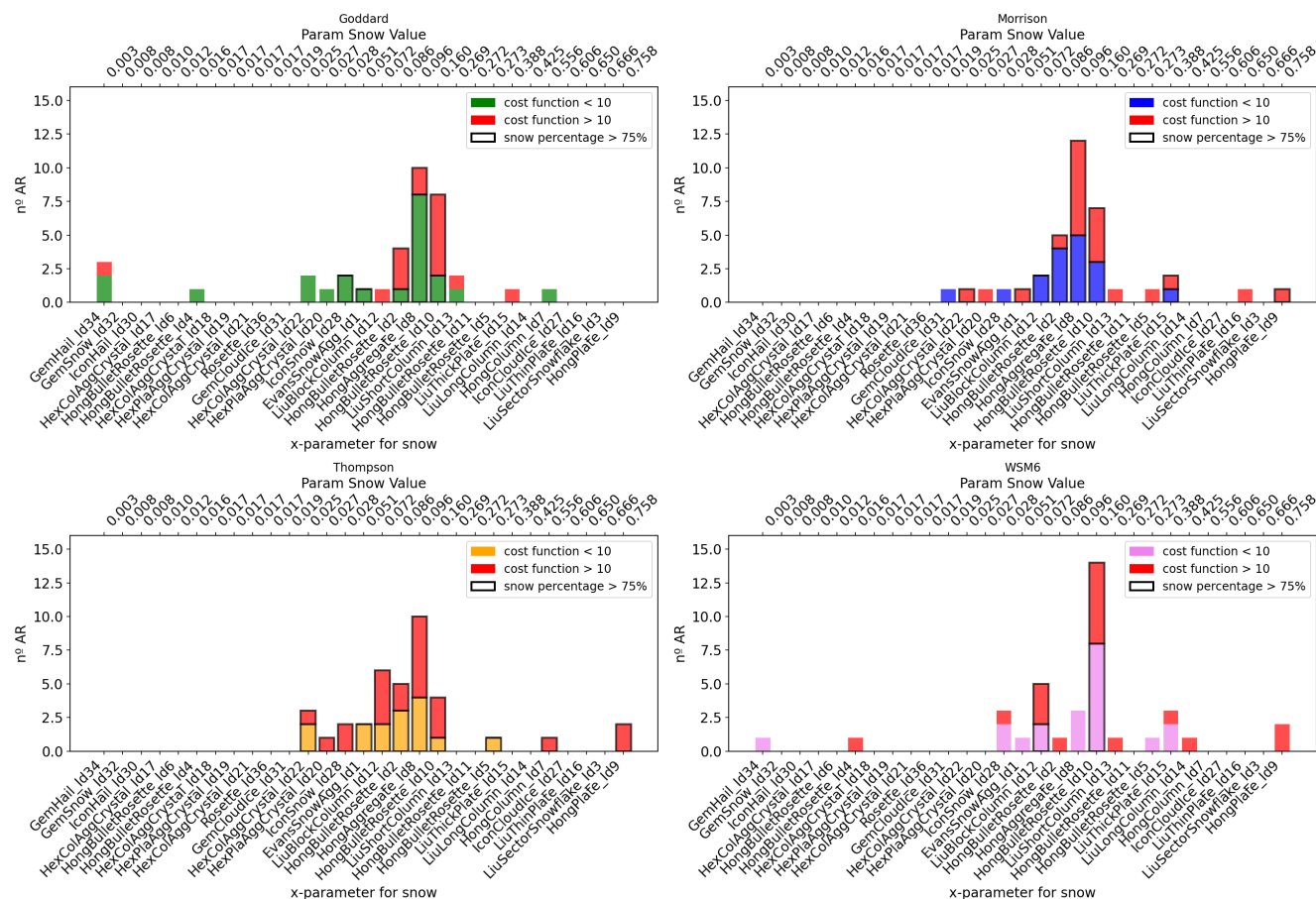
Figure B1. Histograms showing the particles for snow resulted from the optimization process differentiating between the microphysics schemes.